Supplementary Information

Nonvolatile Nematic Order Manipulated by Strain and Magnetic Field in a Layered Antiferromagnet

Zili Feng *et al.*

(Dated: July 21, 2026)

CONTENTS

I. SAMPLE DEPENDENCE OF TRANSPORT PROPERTIES

Experiments in this work are performed on two different batches of crystals of $CoTa_3S_6$, labeled as A and B respectively. We find that the precise values of T_{N1}, T_{N2}, and T^* can vary slightly from batch to batch while staying consistent (within 0.5 K) within each batch. Supplementary Table I summarizes the transition temperatures for samples used in this work. For Batch-A, $T_{N1} \approx 36.5$ K, $T_{N2} \approx 21$ K, and $T^* \approx 30$ K, while for Batch-B, $T_{N1} \approx 37$ K, $T_{N2} \approx 26$ K, and $T^* \approx 34$ K. The batch-to-batch difference of critical temperatures is likely caused by the variation of Co concentration in the crystals [S1]. Energy Dispersive X-ray (EDX) measurements on representative samples yield Co:Ta:S= $0.87 : 3 : 5.69$ (Batch-A) and Co:Ta:S= $0.93 : 3 : 5.85$ (Batch-B). Crystals from both batches appear to fall into the $x < 0.33$ regime of Co_xTaS_2 [S1] (note the renormalization of chemical formula) and are expected to qualitatively host the same set of phases. We note that in transport, T_{N1} and T_{N2} are determined by $d\rho_{xx}/dT$ and $d\rho_{yy}/dT$ (See for instance inset of Fig. S1(a,d)), while T^* is determined by the onset of resistivity anisotropy in trained states with in-plane field.

Supplementary Table I. **Transition temperatures of samples used in this study.** Transition temperatures for the collinear antiferromagnetic phase (T_{N1}), non-coplanar antiferromagnetic phase (T_{N2}), and nematic phase (T^*) are listed for several samples from two batches. "N/A" indicates that the nematic critical temperature does not show up as a singularity in the measurement performed.

Sample	Batch	Measurement	T_{N1} (K)	T_{N2} (K)	T^* (K)
#A01	A	ρ_{xx}	36.5	20.4	N/A
#A04	A	ρ_{xx}	36.5	20.2	30.8
#A05	A	M_z	36.5	20.5	N/A
#B01	B	ρ_{xx},ρ_{yy}	37.0	26.5	34.0
#B02	B	M_z	37.3	26.4	N/A
#B03	B	M_x	36.9	26.3	N/A
#B04	B	ρ_{yy}	37.1	26.1	34.3
#B05	B	ρ_{yy}	37.2	26.5	N/A

Fig. S1 shows the basic transport properties of one representative sample from each batch. Both samples show sizable anomalous Hall effect below T_{N2}; we define the coercive field of the anomalous Hall hysteresis as H_1 and the field scale at which kinks are observed in both ρ_{xx} and ρ_{yx} as H_c. In Fig. S2, we show the hysteresis with out-of-plane magnetic field at 5 K and 20 K for sample B04 in both magnetization and transport (ρ_{xx}, ρ_{yx}) to illustrate the temperature-evolution of H_c and H_1 . As discussed in the main text, we attribute H_c to be the field scale separating low field nematic phase and high field rotation-symmetric phase. Notably, the relative strength of H_c with respect to H_1 can evolve strongly with temperature: from Fig. S2 one can see that H_1 decreases rapidly upon warming, while H_c remains nearly constant between 2 K and 20 K.

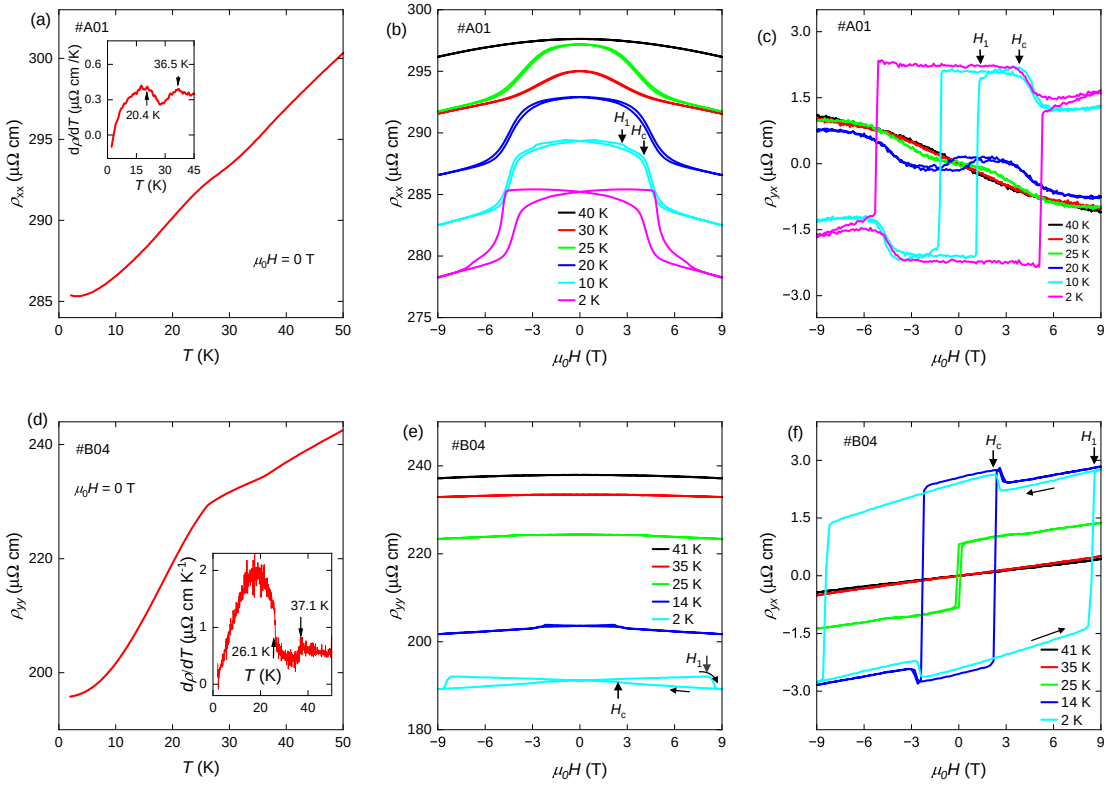

FIG. S1. **Transport properties of Sample** $\#A01$ **and** $\#B04$. (a)(d) Temperature dependence of ρ_{xx} at zero field. The inset shows $\mathrm{d}\rho/\mathrm{d}T$ as a function of temperature. (b)(e) Magnetoresistance under $H \parallel z$ at different temperatures. (c)(f) Hall resistivity ρ_{yx} under $H \parallel z$ at different temperatures.

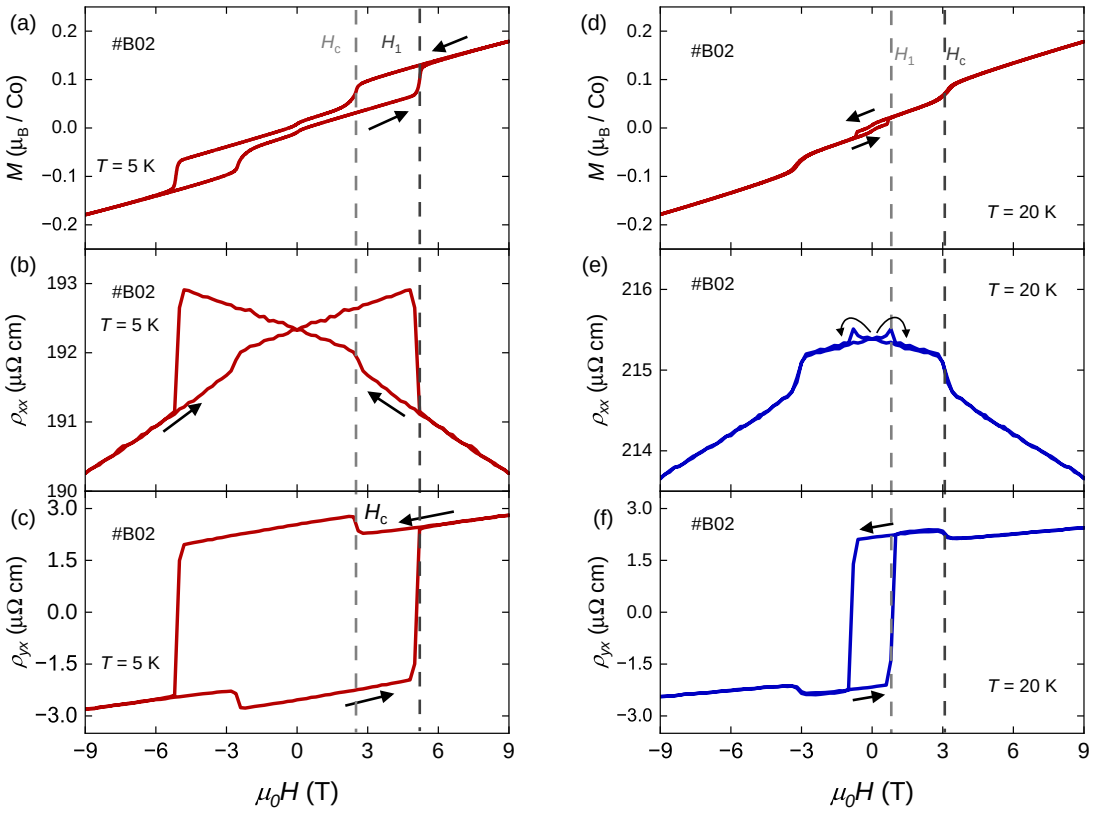

FIG. S2. **Distinction between the magnetic coercivity H_1 and critical field H_c.** $M - H$,$\rho_{xx} - H$, and $\rho_{yx} - H$ for #B02 at $T = 5$ K (a-c), and at T=20 K (d-f).

II. POLARIZATION ROTATION MEASUREMENT

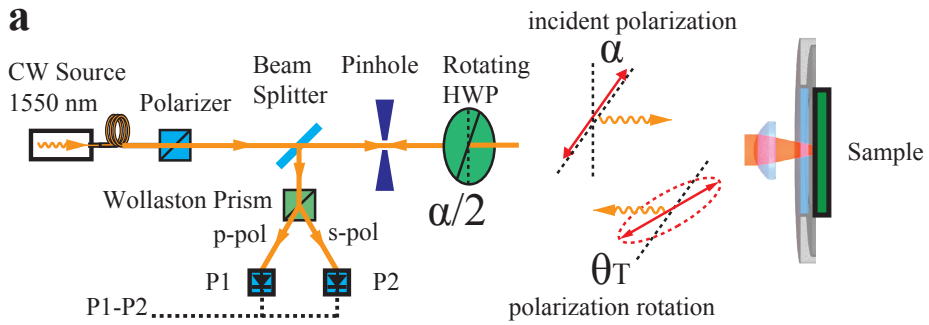

FIG. S3. **Polarization rotation setup operating with continuous-wave (CW) light at 1550 nm wavelength.** (a) Schematics of polarization rotation setup based on a Wollaston prism that measures polarization rotation θ_T as a function of incident polarization α, which is achieved by rotating a half-wave plate (HWP) by $\alpha/2$. The schematics are created with Adobe Illustrator.

The schematic of the optical set up is shown in Fig. S3. A detailed description of the setup can be found in Methods. Fig. S4 and Fig. S5 show respective polar plots of optical polarization rotation θ_T at A and B domain regions at various temperatures, and the solid lines are fits to $\theta_T = \theta_P \sin[2(\alpha - \alpha_0)]$ with θ_P and α_0 as fitting parameters. The extracted θ_P is summarized in Fig. S6 and also main text Fig. 1(h). With an error bar taking into account the fluctuation of α_0 the principal axes for the two domains differ from each other by approximately 120°

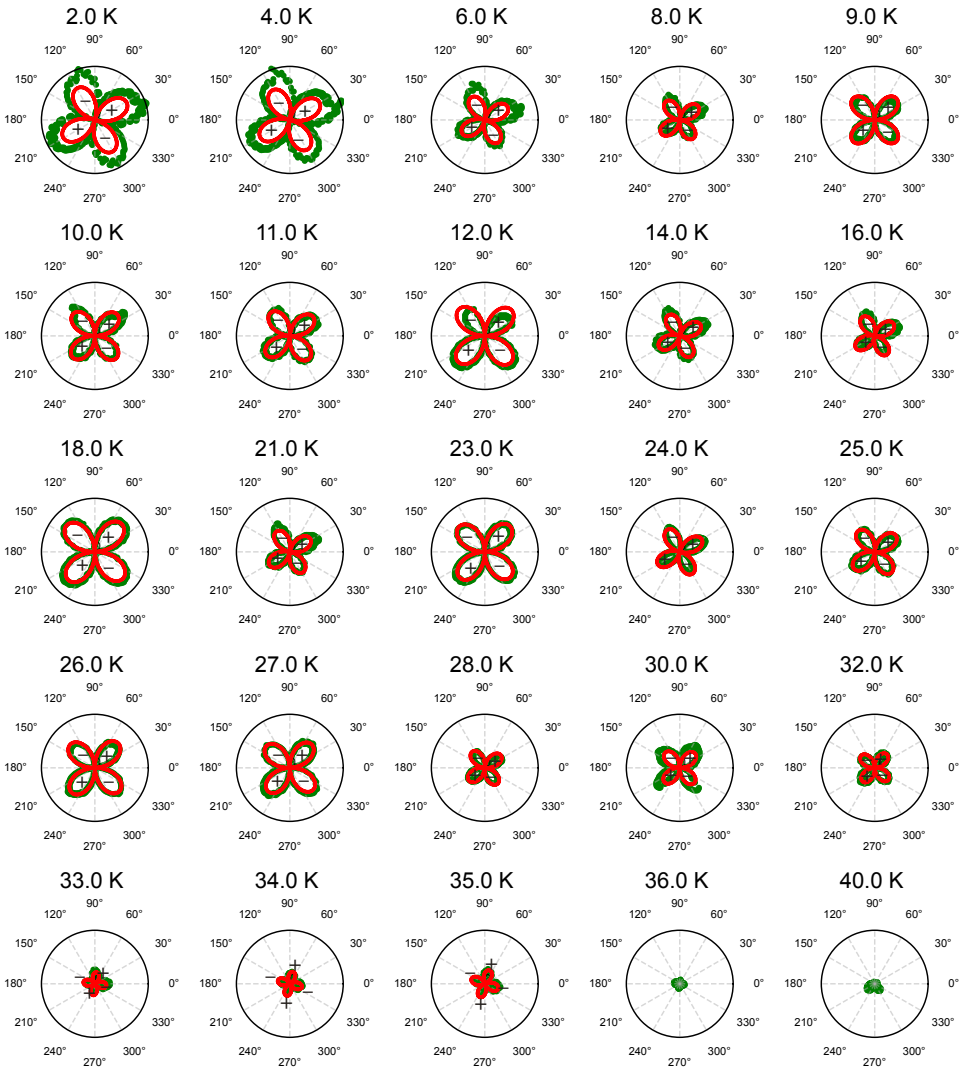

FIG. S4. **Polar plots of optical polarization rotation (θ_T) as a function of the incident light polarization angle α measured at various temperatures inside the A domain.** α is defined so that $\alpha = 0$ corresponds to the light polarization along the x axis. The development of four-leaf clover pattern with alternating "+" and "-" signs indicates birefringence due to the local nematicity. The full scale of the polar plots is 800 μrad.

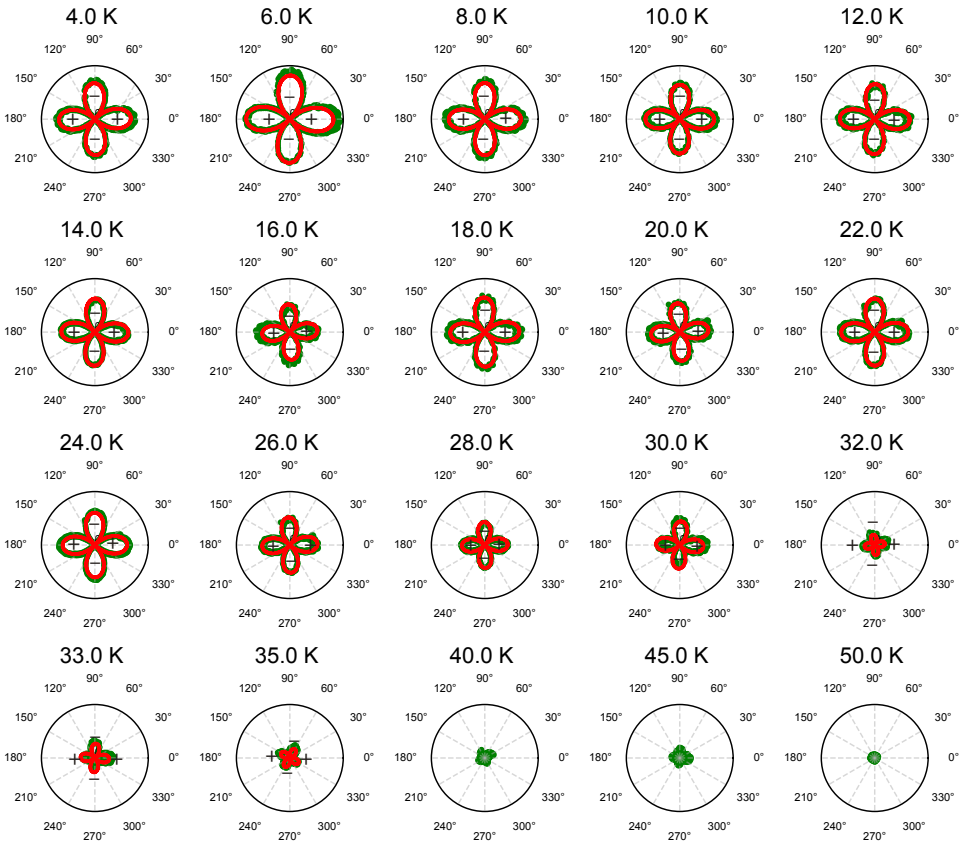

FIG. S5. **Polar plots of optical polarization rotation measured at various temperatures inside the B domain.** The development of four-leaf clover pattern with alternating "+" and "-" signs indicates local anisotropy. The full scale of the polar plots is 800 μrad.

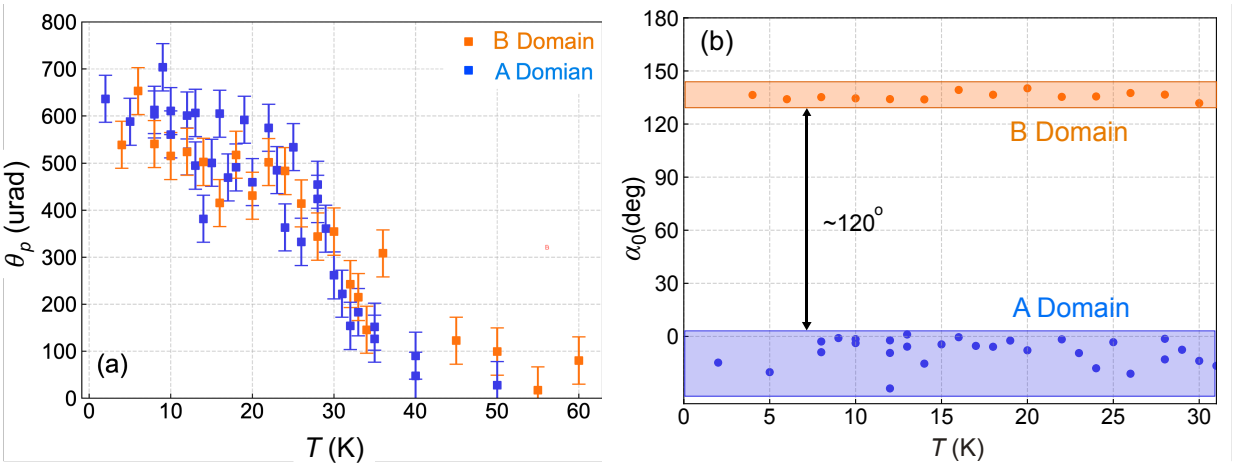

FIG. S6. **Temperature dependence of birefringence amplitude in A and B domains** (a) Fitted birefringence-rotation amplitude θ_P from measurements at various temperatures, blue: A domain, orange: B domain. (b) Fitted nematic director angle α_0 from measurements at various temperatures, blue: A domain, orange: B domain.

III. LANDAU FREE ENERGY ANALYSIS FOR $COTA_3S_6$

A. Magnetic Order

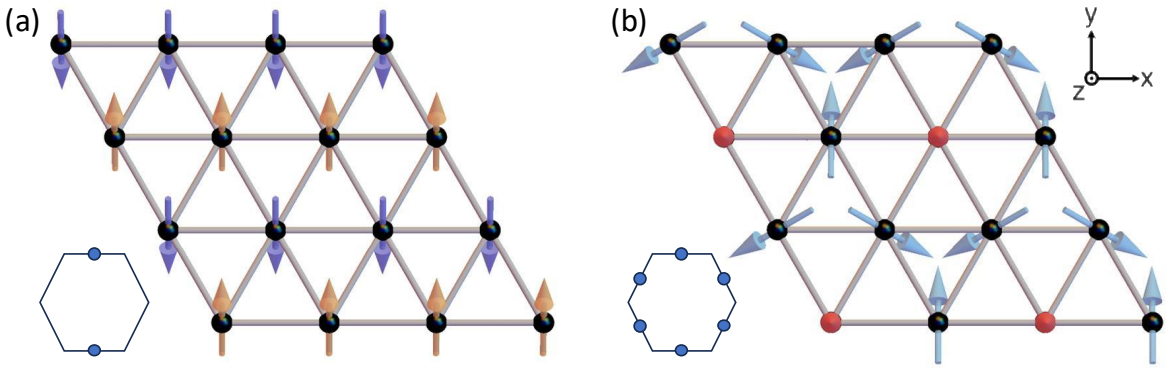

FIG. S7. **Magnetic structures of $CoTa_3S_6$ associated with single-q and triple-q phases** (a) Top view of the single-q collinear AFM state for $\mathbf{Q}_3$ between T_{N1} and T_{N2}. (b) Top view of the non-coplanar triple-q state below T_{N2}. Lower-left insets show the 2D structural Brillouin zone (black hexagon) and the locations of the corresponding magnetic Bragg peaks.

The space group for $CoTa_3S_6$ is $P6_322$, and the point group embedded in the space group is D_6, which is generated by six-fold rotation along c-axis (C_{6z}), and a two-fold rotation along in-plane x-axis (C'_{2x}). Here, we use the point group to constrain the Landau Free energy.

Earlier studies [S2–S4] show that the compound undergoes two magnetic phase transitions – from a paramagnet to a stripe ordered state (Fig. S7(a)) at $T_{N1} \approx 37$ K, and from the stripe state to a non-coplanar state (Fig. S7(b)) at $T_{N2} \approx 26$ K. These magnetic states are schematically shown in Fig. S7. Our study shows that in-between T_{N1} and T_{N2}, nematic order develops. Furthermore, neutron scattering studies show that the stripe state and non-coplanar state are single-q and triple-q states, where the wave vector $\mathbf{Q}$ corresponds to the M-points of the hexagonal Brillouin zone. The AHE observed below T_{N2} may also be understood as originating from electrons coupling with the triple-q magnetic order. The phase transitions at T_{N1} and T_{N2} can be described phenomenologically by the Landau free energy in terms of the Néel vectors $\mathbf{L}_i$ propagating along $\mathbf{Q}_i$ ($i = 1, 2, 3$) at the three M-

points as

$$F_{\text{mag}} = a\sum_{i=1}^{3}\mathbf{L}_i^2 + v_0\left(\sum_{i=1}^{3}\mathbf{L}_i^2\right)^2 + v_1\sum_{i<j}\mathbf{L}_i^2\mathbf{L}_j^2 + v_2\sum_{i<j}\left(\mathbf{L}_i\cdot\mathbf{L}_j\right)^2. \tag{S1}$$

Here we use the definition and convention similar as [S5]. Within a Co layer, a general spin configuration can be expressed as $\mathbf{S}(\mathbf{R}) = \sum_{\mathbf{q}}\mathbf{S}(\mathbf{q})e^{i\mathbf{q}\cdot\mathbf{R}}$. The triple-$q$ order is characterized by three ordering vectors corresponding to the $\Gamma - M$ directions of the hexagonal Brillouin zone:

$$\mathbf{Q}_1 = \frac{\pi}{\sqrt{3}a}(\sqrt{3},1), \quad \mathbf{Q}_2 = \frac{\pi}{\sqrt{3}a}(-\sqrt{3},1), \quad \mathbf{Q}_3 = \frac{\pi}{\sqrt{3}a}(0,-2). \tag{S2}$$

We define Néel vectors $\mathbf{L}_i = \mathbf{S}(\mathbf{Q}_i)$ to describe the magnetic structure of $CoTa_3S_6$.

To account for the non-coplanar triple-q state, we assume $v_2 > 0$ in the temperature range of our interest, thus the ground state should favor $\mathbf{L}_i\cdot\mathbf{L}_j = 0$ for $i \neq j$. When $a < 0$, the ground state $\mathbf{L}$ should take nonzero values. When $v_1 > 0$, single-Q order is favored, and when $v_1 < 0$, triple-Q order is favored [S6]. The v_0 term is an isotropic quartic term that stabilizes the Landau free energy and sets the overall magnitude of the magnetic order parameter. To model the magnetic phase transitions in the two stages, the coefficients in F_{mag} should satisfy $a = \tilde{a}(T - T_{N1}), v_1 = \tilde{v}_1(T - T_{N2}), v_0 > 0, \tilde{a} > 0, \tilde{v}_1 > 0, v_2 > 0$.

The scalar spin chirality of the triple-q magnetic order is given by $\chi = |\mathbf{S}_i\cdot(\mathbf{S}_j\times\mathbf{S}_k)|$ which is proportional to the solid angle spanned by nearest neighbor spins $\mathbf{S}_i$, $\mathbf{S}_j$ and $\mathbf{S}_k$. It could be further written as:

$$\begin{aligned}
|\chi| &= |\mathbf{S}_i\cdot(\mathbf{S}_j\times\mathbf{S}_k)| \\
&= |[(\mathbf{L}_1+\mathbf{L}_2+\mathbf{L}_3)\times(\mathbf{L}_1-\mathbf{L}_2-\mathbf{L}_3)]\cdot(-\mathbf{L}_1+\mathbf{L}_2-\mathbf{L}_3)| \\
&= |-2(\mathbf{L}_1\times\mathbf{L}_2+\mathbf{L}_1\times\mathbf{L}_3)\cdot(-\mathbf{L}_1+\mathbf{L}_2-\mathbf{L}_3)| \\
&= |4(\mathbf{L}_1\times\mathbf{L}_2)\cdot\mathbf{L}_3| \propto |\mathbf{L}_1|\cdot|\mathbf{L}_2|\cdot|\mathbf{L}_3|\,.
\end{aligned} \tag{S3}$$

In the last line, we use the assumption that $\mathbf{L}_1$, $\mathbf{L}_2$ and $\mathbf{L}_3$ are orthogonal with respect to each other that minimizes the v_2 term. As a result, we use $|\mathbf{L}_1|\cdot|\mathbf{L}_2|\cdot|\mathbf{L}_3|$ as a proxy for the non-coplanar AFM order parameter in the main text.

B. Nematic order

We consider the origin of the nematic order observed in experiments. As the nematic order onsets at a temperature *below* T_{N1} – transition temperature for the stripe order – it

is unlikely that the nematic order is a vestigial order of stripe magnetism. Here, we assume that the nematic and magnetic order are of independent origins, but are weakly coupled. We write down the symmetry allowed Free energy for nematicity and nematicity-magnetism coupling. For D_6 point group, the nematic order is two-component, and transforms as E_2 irreducible-representation (irrep) [S7]. It is convenient to parametrize the two-component order parameter as $(n_1, n_2) = n\,(\cos 2\theta, \sin 2\theta)$, where θ is the orientation of the nematic director measured from the x axis. The factor of two in 2θ ensures that the nematic order is a director, not a vector [S5, S8], i.e., θ and $\theta + \pi$ are the same state. To find the coupling between n and $\mathbf{L}$, we note that $(\mathbf{L}_1^2 + \mathbf{L}_2^2 - 2\mathbf{L}_3^2, \mathbf{L}_1^2 - \mathbf{L}_2^2)$ transforms in E_2 irrep and is time-reversal even. Symmetry analysis of the transformation matrix shows that the nematicity-magnetism coupling reads $n_1(\mathbf{L}_1^2 + \mathbf{L}_2^2 - 2\mathbf{L}_3^2) + n_2(\mathbf{L}_1^2 - \mathbf{L}_2^2)$. With these considerations, the Landau Free energy for nematic order (parametrized by n, θ) reads

$$F_{\rm n} + F_{\rm n-mag} = bn^2 + cn^3 \cos 6\theta + wn^4 + gn\left(\cos 2\theta(\mathbf{L}_1^2 + \mathbf{L}_2^2 - 2\mathbf{L}_3^2) + \sin 2\theta\sqrt{3}(\mathbf{L}_1^2 - \mathbf{L}_2^2)\right), \tag{S4}$$

where the first three terms, defined as $F_{\rm n}$, are the Free energy for the three-states Potts model. We set $c < 0$, so the nematic director takes value $\theta = \pi/3, -\pi/3, 0$ to minimize $F_{\rm n}$. To describe the nematic phase transition, we have $b = \tilde{b}(T - T_n), w > 0$. Due to $g \neq 0$, the nematic order can be induced by the stripe order at T_n right below T_{N1}. Here, we assume $g > 0$ so that there is no frustration for the nematicity pinned by the stripe order and the one by the c-coefficient.

By minimizing $F = F_{\rm mag} + F_{\rm n} + F_{\rm n-mag}$, we find the nematic order parameter, spin-chirality and magnetic order parameter v.s. temperature. To demonstrate how the underlying magnetic structures are coupled to the nematic domain, we examine the ground state $\mathbf{L}_i$ from minimizing the Landau free energy model, assuming single nematic domain population ($\theta = 0, \pi/3, -\pi/3$). With the coupling term $F_{\rm n-mag}$, below T_{N2} near zero magnetic field, we obtain an anisotropic triple-q state with $|\mathbf{L}_1| : |\mathbf{L}_2| : |\mathbf{L}_3| \sim 1 : 1 : 1.01$ for a given nematic domain $\theta = 0$, and $|\mathbf{L}_1| : |\mathbf{L}_2| : |\mathbf{L}_3| \sim 0 : 0 : 1$ between T^* and T_{N2}. The result shows that the nematic director $\theta = 0$ favors a larger $|\mathbf{L}_3|$ out of the triple-q components. Similarly, we find that nematic director $\theta = \pi/3$ favors $|\mathbf{L}_2|$, and that $\theta = -\pi/3$ favors $|\mathbf{L}_1|$.

IV. IN-PLANE RESISTIVITY ANISOTROPY MEASURED BY MODIFIED MONTGOMERY METHOD

To properly illustrate the resistivity anisotropy of $CoTa_3S_6$ and eliminate the effect of sample shape-dependence, a modified Montgomery method [S9–S11] is used to measure ρ_{xx} and ρ_{yy} simultaneously in the same sample. The sample is polished into a thin and rectangular-shape with L_x= 1.333 mm, L_y= 1.180 mm and L_z=0.044 mm, as shown in the inset of Fig. S8(a). The resistance R_{xx} (R_{yy}) is obtained by applying current I_x (I_y) along x (y) axis on one side of the sample, and measuring the voltage difference V_x (V_y) along the same axis on the other side. ρ_{xx} and ρ_{yy} are subsequently calculated based on the following equations:

$$\rho_{xx} = \frac{\pi}{8}\left(\frac{L_z L_y}{L_x}\right)\left(\frac{L'_x}{L'_y}\right) R_{xx} \sinh\left(\frac{\pi L'_y}{L'_x}\right), \tag{S5}$$

$$\rho_{yy} = \frac{\pi}{8}\left(\frac{L_z L_x}{L_y}\right)\left(\frac{L'_y}{L'_x}\right) R_{yy} \sinh\left(\frac{\pi L'_x}{L'_y}\right), \tag{S6}$$

$$\frac{L'_y}{L'_x} \approx \frac{1}{2}\left[\frac{1}{\pi}\ln\frac{R_{yy}}{R_{xx}} + \sqrt{\left(\frac{1}{\pi}\ln\frac{R_{yy}}{R_{xx}}\right)^2 + 4}\right]. \tag{S7}$$

ρ_{xx} and ρ_{yy} shown in Fig. S8(b) are the zero-field cooled (ZFC) resistivities measured at zero field upon warming, i.e., ρ_{ii}(ZFC) for $i = x, y$. These are comparable with that measured by standard four-probe method shown in Fig. S1(b). Fig. S8(c) shows the ratio ρ_{xx}/ρ_{yy} as a function of temperature. Over the entire temperature range, the ratio is around 1 (with an error about 0.7%), indicating that a multi-domain state is realized to mask to nematicity below T^* and misalignment of sample shape and electrodes is negligible. We note that Eqs. (S5)-(S6) are derived under the assumption of a diagonal resistivity tensor [S9, S10]. When the nematic director is not aligned along the x or y axis, the off-diagonal components ($\rho_{xy} = \rho_{yx}$) becomes finite. Nevertheless, applying the current formula remains valid because the resistivity anisotropy is not so large. Estimating the diagonal resistivities by Eqs. (S5)-(S6) introduces an error of at most 0.03% by neglecting the off-diagonal terms [S12].

Fig. S8(d-f) show how anisotropic ρ_{xx} and ρ_{yy} of the field-trained state evolve with temperature and out-plane magnetic field, which is obtained by field cooling under $\mu_0 H$ = 9 T

along x-axis. Compared with resistivity in the ZFC state, shown in Fig. S8(b), ρ_{xx} and ρ_{yy} becomes considerably different after magnetic field cooling (Fig. S8(d)). Fig. S8(e) shows that a moderate out-plane magnetic field ($\sim$ 3 T) can cause the resistivity anisotropy to collapse. Fig. S8(d) and (e) are the raw data of Fig. 1(e) and Fig. 4(a) in the main text where the ratio $\tilde{\rho}_{ii} \equiv \rho_{ii}(\mathrm{FC})/\rho_{ii}(\mathrm{ZFC})$ is shown for clarity. Fig. S8(f) shows $\tilde{\rho}_{xx} - \tilde{\rho}_{yy}$ as a function of out-plane magnetic field at selected temperatures. Before field scan at each target temperature, the system is cooled to 2 K under in-plane magnetic field $\mu_0 H = 9$ T along x axis and then warmed up to the target temperature under zero magnetic field. The phase diagram shown in Fig.4(b) in the main text is constructed from data shown in Fig. S8(f).

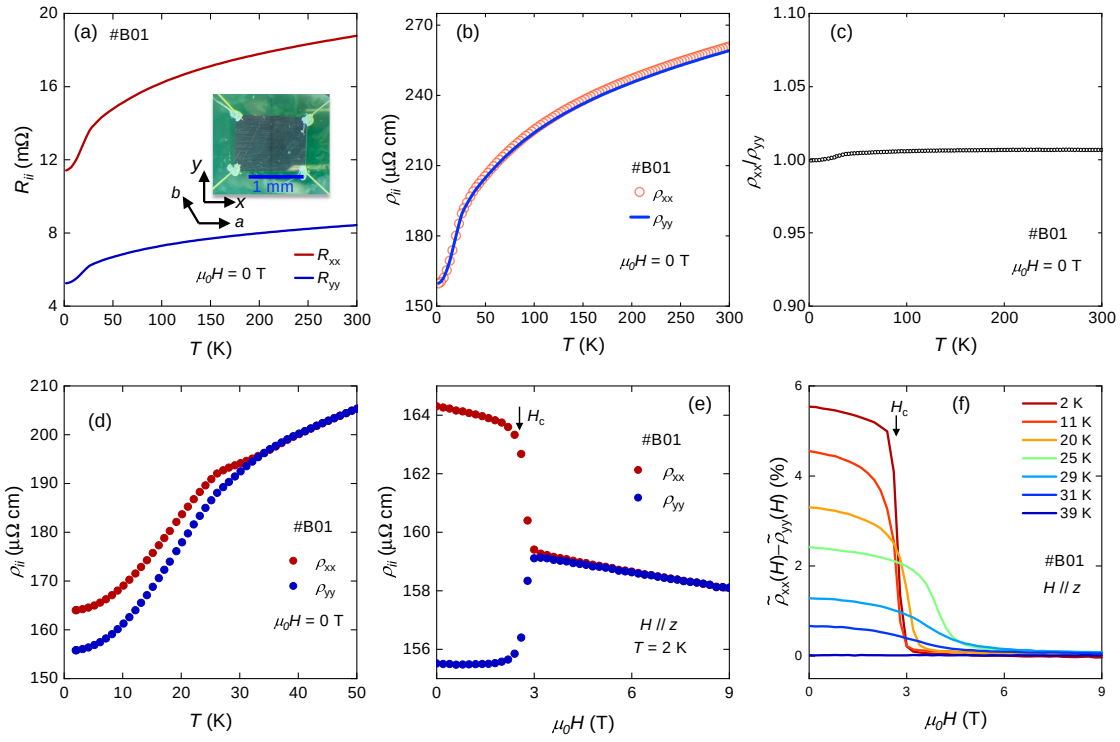

FIG. S8. **Evaluation of in-plane resistivities by the Montgomery method** (a) Temperature dependence of resistances R_{xx} and R_{yy} at zero field. The inset is an optical image of sample used for the measurement. The scale bar is 1 mm. (b,c) ρ_{xx} and ρ_{yy} for a zero-field cooled state obtained from R_{xx} and R_{yy} by Eqs. S5-S7 (b) and the corresponding ratio ρ_{xx}/ρ_{yy} (c). (d-e) Temperature- (d) and out-of-plane magnetic field- (e) evolution of ρ_{xx} and ρ_{yy} of the field-trained state, where 9 T of $H \parallel x$ is used for training. (f) Out-of-plane magnetic field dependence of $\tilde{\rho}_{xx} - \tilde{\rho}_{yy}$ under the field-trained state at various temperatures.

V. STRAIN TUNING OF RESISTIVITY ANISOTROPY AT 10 K

Fig. S9 shows the strain effect on ρ_{xx} at $T = 10$ K, which is qualitatively consistent with that at $T = 2$ K shown in the main text. The inset of Fig. S9(b) shows the linear dependence of $\rho_{xx}(9\ \mathrm{T})$ as a function of strain while the zero field ρ_{xx} illustrated in the form of MR $= \frac{\rho_{xx}(0\ \mathrm{T})-\rho_{xx}(9\ \mathrm{T})}{\rho_{xx}(9\ \mathrm{T})}$ is compared to a guideline to the eye (Fig. S9(b)). Distinct from the behavior at $T = 2$ K, the coercive field H_1 is smaller than the critical field H_c at $T = 10$ K. This enable us to clarify the relationship between nematic order and the characteristic magnetic fields in the system: the nonlinear strain-dependence of ρ_{xx} is correlated with H_c instead of the coercive field H_1, suggesting that H_c is the field scale associated with the observed rotation symmetry breaking.

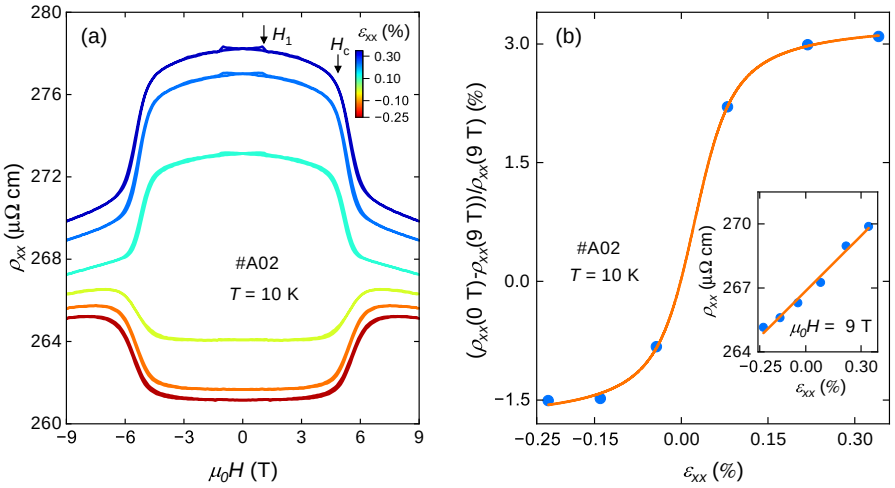

FIG. S9. **Strain-evolution of resistivity at $T = 10$ K** (a) Out-of-plane magnetic field dependence of ρ_{xx} measured at $T = 10$ K under various strain ϵ_{xx}. (b) Strain dependence of the magnetoresistance: MR = ($\rho_{xx}(0\ \mathrm{T})$ - $\rho_{xx}(9\ \mathrm{T})$)/$\rho_{xx}(9\ \mathrm{T})$ (blue circles). Orange curve is a guideline to the eye. Inset is the strain dependence of $\rho_{xx}(9\ \mathrm{T})$. Orange solid line is a linear fitting.

VI. IN-PLANE FIELD AS CONJUGATE FIELD TO NEMATIC ORDER

Here we present additional evidence that in-plane magnetic fields, in particular in the form of $H_x^2 - H_y^2$, which has the same symmetry with $\epsilon_{xx} - \epsilon_{yy}$ and $\sigma_{xx} - \sigma_{yy}$, can serve as a 'training' conjugate field to the nematic order in $CoTa_3S_6$. A standard four terminals method is adopted for measuring ρ_{xx} and Hall resistivity ρ_{yx} simultaneously. Current is applied along x and magnetic field within the xz or yz plane. With varying the magnetic field angles θ_1 (defined from z with rotation within the xz plane) and θ_2 (defined from z with rotation within the yz plane), we intend to tune the component of in-plane fields H_x and H_y and thereby test the effect of $H_x^2 - H_y^2$ as a training field.

To focus on the nematic phase, we limit the following discussions on the phase near zero field. Fig. S10(a) and (b) show that with increasing θ_1 (θ_2), which consequently increases the maximum H_x (H_y) as a training field, ρ_{xx} (0 T) increases (decreases). The effect of H_x (H_y) is consistent with trends demonstrated by the Montgomery method shown in main text Fig. 3. In Fig. S10(c), $\rho_{xx}(\theta_1,\theta_2)/\rho_{xx}(\theta_1 = 0,\theta_2 = 0)$ at zero magnetic field after 'training' with respective H_x and H_y is plotted as a function of the maximal $H_x^2 - H_y^2$ achieved during field scan. Owing to re-mounting of the sample while changing the field rotation from xz plane to yz plane, ρ_{xx}(0 T) with field along z is slightly different. We normalize $\rho_{xx}(\theta_1, \theta_2)$ to the respective $\rho_{xx}(\theta_1 = 0,\theta_2 = 0)$ at zero magnetic field. The evolution of ρ_{xx}(0 T) can be described by a a modified Langevin function (red solid curve) often used to describe the polarization process of ferromagnets [S13].

Fig. S10(d,e) shows the anomalous Hall resistivity ρ_{yx} at zero field with various magnetic field directions. ρ_{yx} at zero magnetic field barely changes with the direction of in-plane magnetic fields (θ_1, θ_2) as summarized in Fig. S10(f). This indicates that the anomalous Hall domains are likely purely aligned by the z-component of magnetic field when the field is tilted away from z, and that the nematic order (domain) that couples to in-plane magnetic field and strain is independent to the anomalous Hall effect ρ_{yx} in the system.

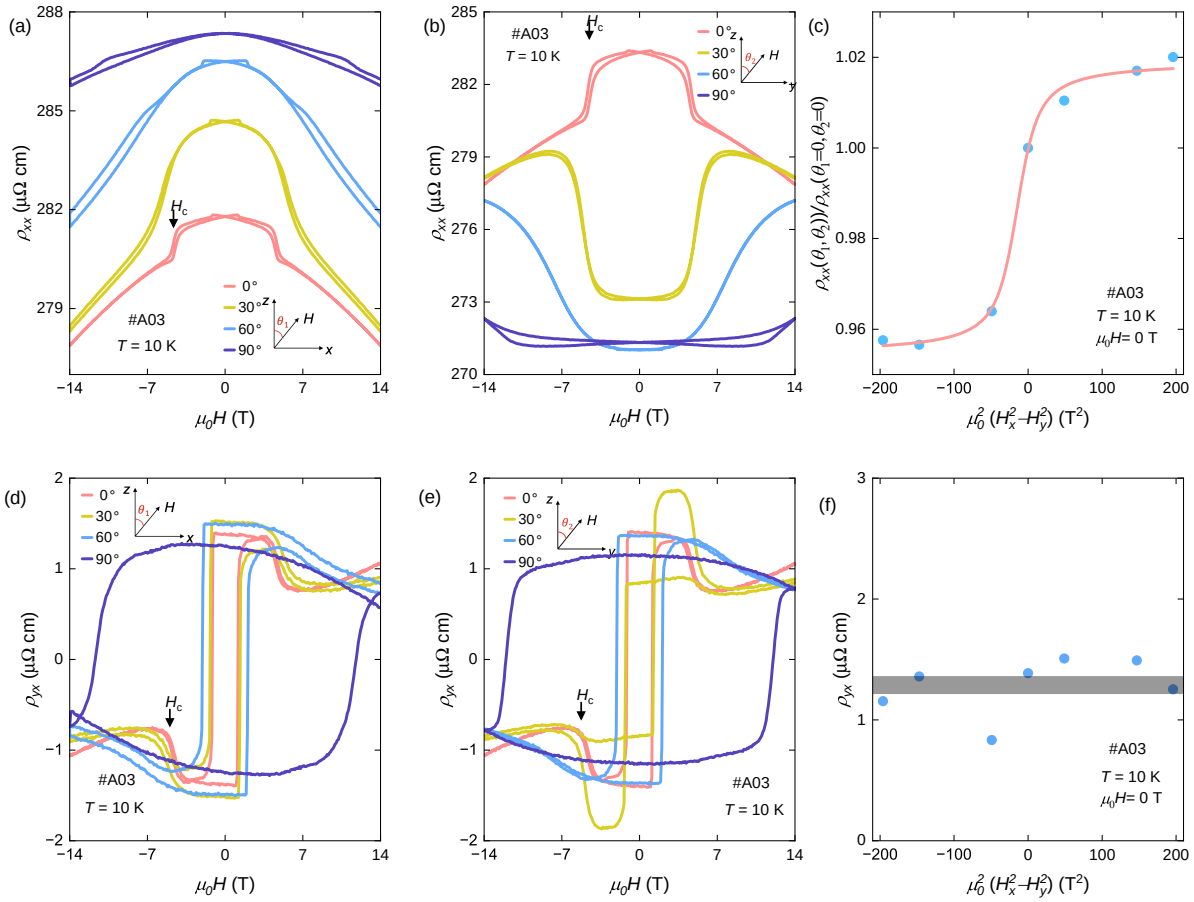

FIG. S10. **Transport of $CoTa_3S_6$ with canted magnetic field configuration** (a,b) Magnetoresistance ρ_{xx} taken with selected magnetic field angles. The current is applied along x in both (a) and (b). The magnetic field is rotated from out-of-plane to in-plane and parallel to the current in (a, θ_1 rotation) and from out-of-plane to in-plane but perpendicular to the current (b, θ_2 rotation). (c) ρ_{xx}(0 T) normalized to that from field scan with out-of-plane field only (virgin for in-plane field) as a function of the maximum in-plane training fields $H_x^2 - H_y^2$ for the field scans shown in (a) and (b). The normalized ρ_{xx}(0 T) can be fitted by a modified Langevin function (red curve). (d,e) Hall resistivity ρ_{yx} under different field angles corresponding to (a) and (b), respectively. (f) Zero field anomalous Hall resistivity ρ_{yx} as a function of in-plane training field $H_x^2 - H_y^2$. The gray bar is a horizontal guideline to the eye.

VII. MANIPULATION OF RESISTIVITY ANISOTROPY IN THE PRESENCE OF BOTH IN-PLANE STRAIN AND MAGNETIC FIELD

Fig. S11(a) shows the in-plane magnetic field dependence of ρ_{yy} where both magnetic field and stress are applied along y. Since electric current is parallel with magnetic field, no orbital magnetoresistance is expected. Under tensile strains (blue curves in Fig. S11(a)), a weak negative magnetoresistance is observed and likely originates from suppression of spin fluctuation under magnetic field. In contrast, ρ_{yy} exhibits sharp hysteresis and a step-like increase at a characteristic field scale H_T under compressive strains (see red, orange and yellow curves in Fig. S11(a)). The hysteretic regime is highlighted in the color plot of $\rho_{yy}(H,\uparrow) - \rho_{yy}(H,\downarrow)$ (difference in ρ_{yy} in field-up and field-down scans) in the $H_y - \epsilon_{yy}$ phase space in Fig. S11(b). In Fig. S11(c) we summarize our hypothetical configurations of nematic domains in the $H_y - \epsilon_{yy}$ phase space: positive H_y and positive ϵ_{yy} cooperate to select the domains corresponding to higher ρ_{yy} shown in inset. This is consistent with our overall observation that both in-plane tensile strain and magnetic fields prefer nematic domains with higher resistivity along the tensile strain/field direction.

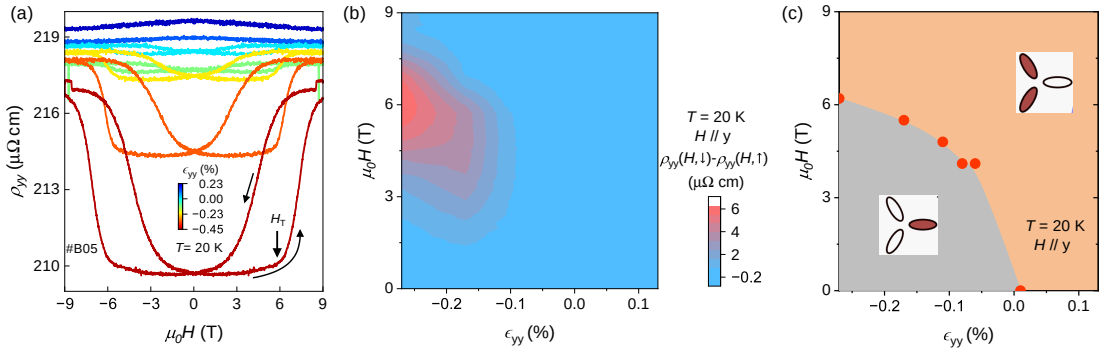

FIG. S11. **H_y-ϵ_{yy} phase diagram for $CoTa_3S_6$** (a) Magnetic field dependence of ρ_{yy} under various strains at $T = 20$ K. Uniaxial stress and magnetic field are both applied along y-axis. The black arrow shows the field sweep direction. H_T marks the field where the step-like transition takes place. (b) Color map of $\rho_{yy}(H,\uparrow) - \rho_{yy}(H,\downarrow)$ in the H-ϵ_{yy} phase diagram. $\rho_{yy}(H,\uparrow)$ ($\rho_{yy}(H,\downarrow)$) stands for ρ_{yy} under the magnetic field sweeping from +9 T (−9 T) to −9 T (+9 T). (c) Schematic H-ϵ_{yy} phase diagram. The phase boundary is extracted from the peaks in field dependence of $\rho_{yy}(H,\uparrow) - \rho_{yy}(H,\downarrow)$ at various strains. Inset shows schematic of the active nematic domains with field and strain.

VIII. REVERSIBLE NEMATIC DOMAIN SWITCHING AT VARIOUS TEMPERATURES

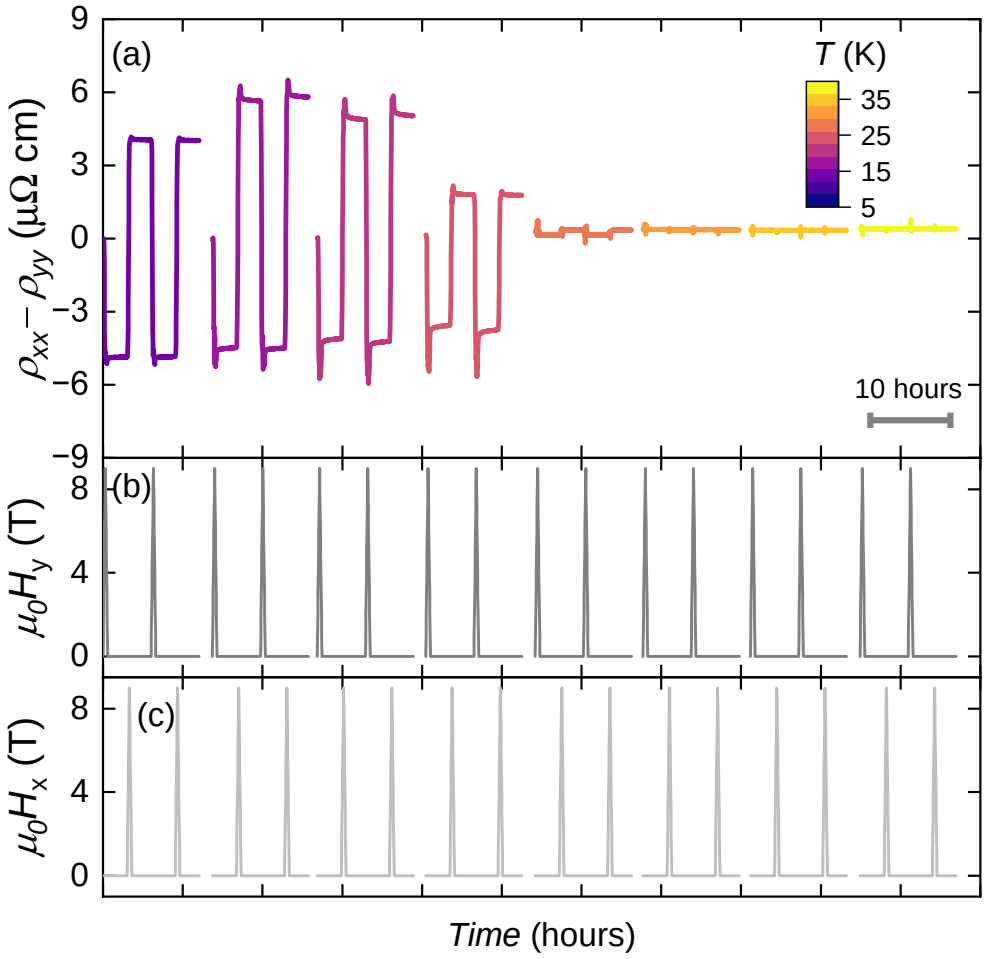

FIG. S12. **Reversible nematic domain switching at various temperatures** (a) Time-dependence of $\rho_{xx} - \rho_{yy}$ with field history shown in (b) and (c). Traces with different colors are taken at different temperatures. The color scale shown in inset of (a). The time-dependence of $\rho_{xx} - \rho_{yy}, H_x, H_y$ in (a-c) are offset horizontally for clarity.

To further evaluate the switching of nematic domains in $CoTa_3S_6$ by in-plane magnetic field, $\rho_{xx} - \rho_{yy}$ is measured by using the Montgomery method with subsequent application of alternating $H \parallel x$ and $H \parallel y$ at various temperatures (Fig. S12). In this set of experiments, the sample was first cooled to the target temperature from 50 K with zero field, and a time sequence of in-plane training field (Fig.S12(b,c)) was applied to switch the nematic domains.

The effect of the switching process is evidenced by $\rho_{xx} - \rho_{yy}$ (Fig.S12(a)), where $H \parallel x$ tends to select domains with $\rho_{xx} - \rho_{yy} > 0$ and $H \parallel y$ domains with $\rho_{xx} - \rho_{yy} < 0$. We note that this process can be repeated and reversed at least multiple times at each temperature with the non-zero plateaus in $\rho_{xx} - \rho_{yy}$ retaining non-volatile nematic memory after removing the training fields. The memory effect is quite sizable up to 20 K and is still finite at 30 K. The spikes in Fig. S12(a) correspond to the volatile portion of the nematic memory in the system.

We note that the 'switched' resistivity anisotropy has a non-monotonic temperature dependence, which we attribute to the temperature-dependence of the thermodynamic barrier between the different nematic domains: at low temperature, the thermodynamic barrier is high, a magnetic field higher than the training field used (9 T) may be required to fully switch the nematic domains; at high temperature, the thermodynamic barrier may be too low to generate a memory effect at zero field.

IX. MAGNETIC FIELD ANGLE DEPENDENCE OF THE NEMATIC DOMAIN SWITCHING

In addition to the optical measurements (SI Sec. III), we further strengthen the experimental evidence for three-state nematic order through transport studies using a device with threefold rotational symmetry. We prepare a single crystal cut into a hexagonal shape with electrodes at each corner (Fig. S13(a)), which enables the simultaneous resistance measurement along three directions 120° away from each other (Channels 1-3). Prior to the measurements, the sample was field-cooled with in-plane magnetic field of 9 T applied along certain directions (θ is defined with respect to the a axis), and then the field was removed at 2 K. Potential contribution from the spontaneous Hall effect and electrode misalignment were corrected by symmetrizing the data with respect to magnetic field. As shown in Fig. S13(b)-(d), the Channel 1 resistance peaks when the cooling field was aligned along the a axis ($\theta = 0°, 180°$). In contrast, channel 2 and 3 take their respective maximum when $\theta = 120°, 300°$ and $\theta = 60°, 240°$. These results suggest the presence of three nematic domains, which can be controlled by the orientation of cooling-field direction.

In Fig. S14 (a-b) we show the respective evolution of ρ_{xx} and ρ_{yy} as the magnetic field is rotated in the xy-plane. The red and blue curves indicate ρ_{ii} obtained with clockwise

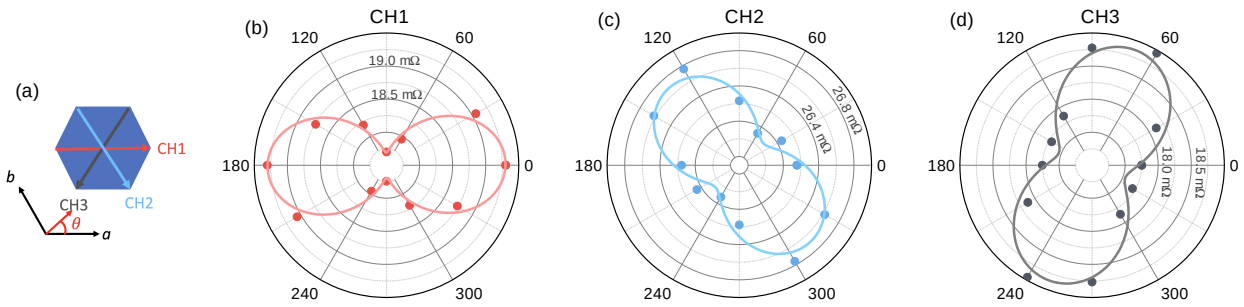

FIG. S13. **Three-state transport anisotropy** (a) Schematic of a hexagonal transport device. Electrodes are attached to the six corners allowing measurement of resistivity along three principal axes 120° away from each other. Red, blue and black arrows indicate current directions for resistivity measurements of channel 1, 2 and 3, respectively. θ is the angle of the applied in-plane magnetic field measured from the a axis. (b-d) Resistance in the three channels at 2 K and zero field. Prior to the measurement, the sample was field-cooled at respective field orientations (θ), as represented by the polar coordinate. $\theta = 0°$ (360°) corresponds to the a axis. The solid curves are fit to $R = R_0 + A\cos(2\theta - \alpha)$, where R_0, A, and α are fitting parameters.

and counterclockwise rotation of the magnetic field, respectively, starting from a field cooled state at $\theta = 0$. Both $\rho_{xx}(\theta)$ and $\rho_{yy}(\theta)$ are composed of a sequence of plateaus, and the width for the low (high) resistivity plateau for ρ_{xx} (ρ_{yy}) is twice as wide as the corresponding high (low) resistivity state. This is consistent with a three-state nematic order in the system, and that in both ρ_{xx} and ρ_{yy}, two out of the three (A vs B, C) is indistinguishable. For CCW rotation in particular, the system starts with a plateau state that spans $\sim 40°$ is high in ρ_{xx} and low in ρ_{yy}, consistent with A domain being most activated here. We therefore attribute an increased resistivity along the long axes of the nematic director. Furthermore, the angular hysteresis shown in Fig. S14(a-b) suggests that the nematic directors appear to be strongly pinned to the principal a and equivalent axes of the crystal and can be rotated only in a discrete manner (one example of such switching process with magnetic field rotation is shown in Fig. S14(c)) with the in-plane magnetic field orientation.

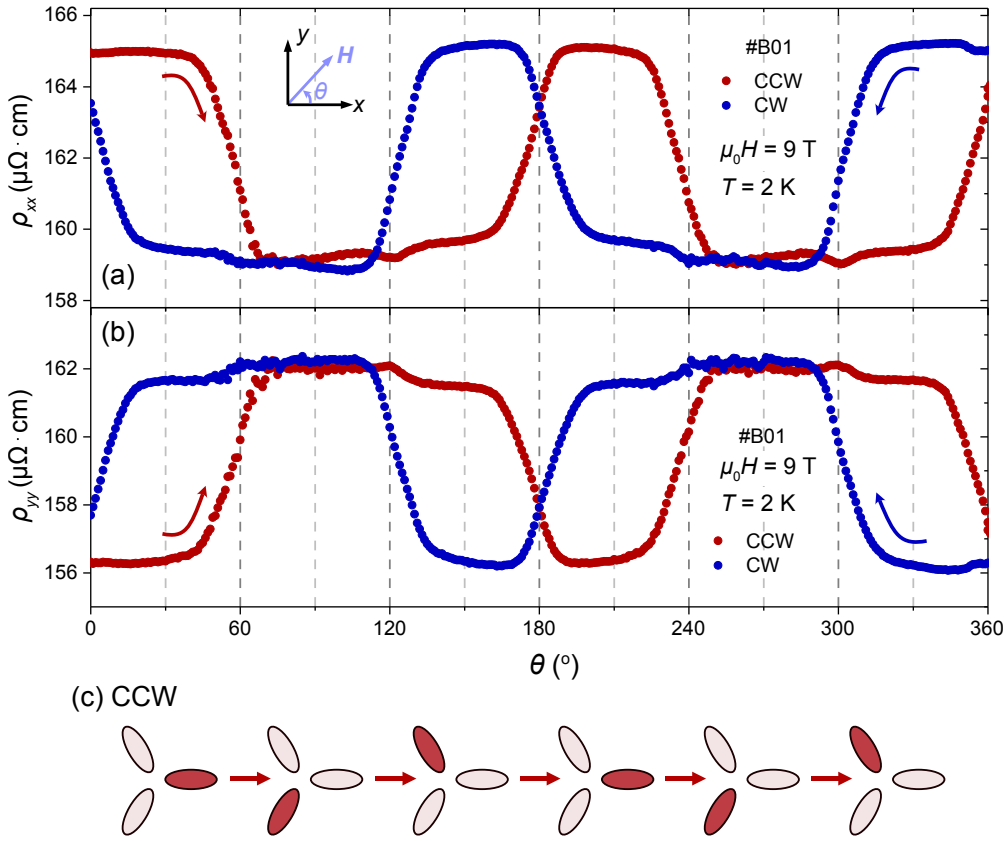

FIG. S14. **Evolution of nematic domains with in-plane magnetic field rotation** (a,b) Angle (θ) dependence of ρ_{xx} and ρ_{yy} under $\mu_0 H = 9$ T. Here θ is defined within the ab plane and $\theta = 0°$ corresponds to the x-axis. Before the angle scan, the sample was prepared with field cooling at $\mu_0 H = 9$ T along the x axis. Blue (red) curves are taken with clockwise (CW) and counterclockwise (CCW) rotation of the magnetic field and the rotation direction is indicated with arrows with corresponding colors. (c) Schematic of domain selection with in-plane magnetic field rotation for the CCW rotation. Darker shade indicate the favored domain at the corresponding angle range labeled by the axis of (b).

X. ASSIGNMENT OF THE ORIENTATION OF NEMATIC DOMAINS

Three different nematic domains are schematically shown in Fig.1(c) in the main text along the principle axis. The assignment of the orientation of nematic domains flowing the discussion below.

It is noted that domain B and domain C can not be distinguished by ρ_{xx} and ρ_{yy}. As for the magnetic field manipulation of the nematic director, red curve in Fig. S14(a) shows two different states, a low-ρ_{xx} state and a high-ρ_{xx} state. The angle range for the low-ρ_{xx} state ($60 < \theta < 180$,$240 < \theta < 360$) is twice of the range for the high-ρ_{xx} state ($0 < \theta < 60$,$180 < \theta < 240$). This is the same for the other three curves in Fig. S14(a,b). This indicates that the domain B and domain C belong to the low-ρ_{xx} state, and the domain A belongs to high-ρ_{xx} state. The later suggests that the nematic director tends to be aligned with the magnetic field. Following this scenario, the magnetic field angle dependence of the nematic domain is plotted in Fig. S14(c). In Fig.3(b) in the main text, when a magnetic field is applied along y-axis, since finite component of the field exist for nematic director B and C, those two domain coexists.

As for the strain manipulation of the nematic director, it is noted that under tensile strain along x-axis,it is at high-ρ_{xx} state which indicates it stays domain A. Correspondingly under compressive strain along x-axis, it is at low-ρ_{xx} state with coexisting domain B and domain C.

XI. NEMATIC TRANSITION UNDER IN-PLANE OR OUT-PLANE MAGNETIC FIELD

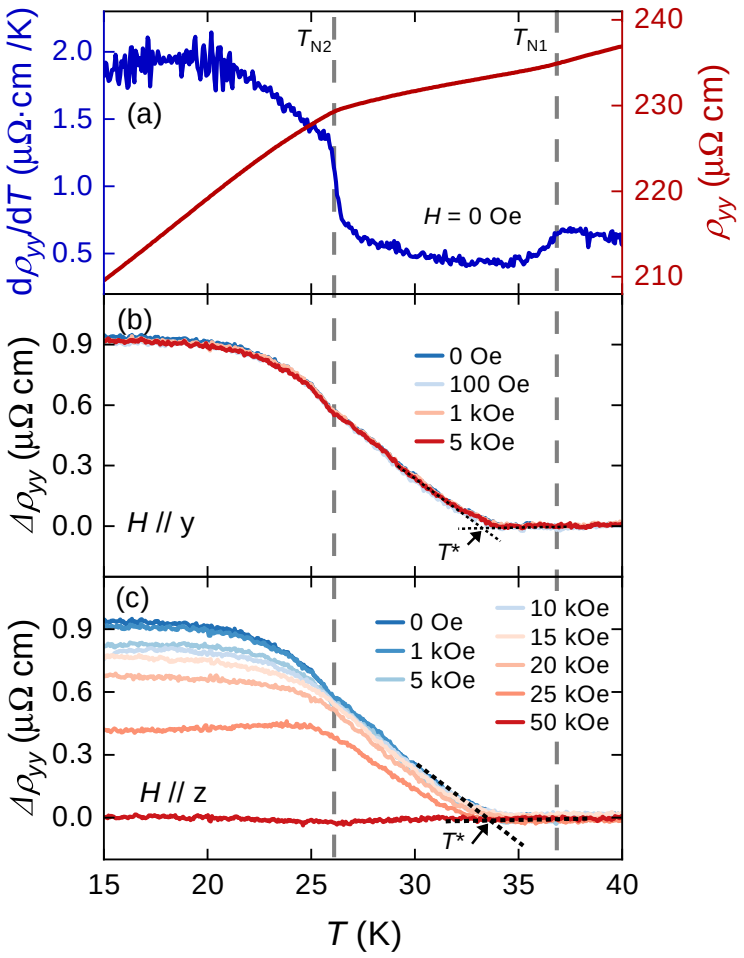

FIG. S15. **Comparison between nematic and magnetic transitions temperatures in a bar-shape sample** All data were measured with a standard four-terminal method. (a) ρ_{yy} measured at zero field (right axis) and the corresponding temperature derivative $d\rho_{yy}/dT$ (left axis). (b,c) $\Delta\rho_{yy} = \rho_{yy}(FC)$-$\rho_{yy}(ZFC)$ (see text) under selected in-plane (b) and out-plane magnetic fields (c). T_{N1} and T_{N2} are indicated by gray dashed lines.

Figure S15 shows the determination of the antiferromagnetic transitions T_{N1} and T_{N2}, and the nematic transition temperature T^* with ρ_{yy} of a zero field-cooled (ZFC) state a field-cooled (FC) state measured through warming respectively. Here different in-plane or out-of-plane magnetic fields are applied. The FC state is obtained by cooling the sample from 50 K to 2 K under $\mu_0 H$=9 T along y. In Fig. S15(a), ZFC resistivity ρ_{yy} shows two kinks

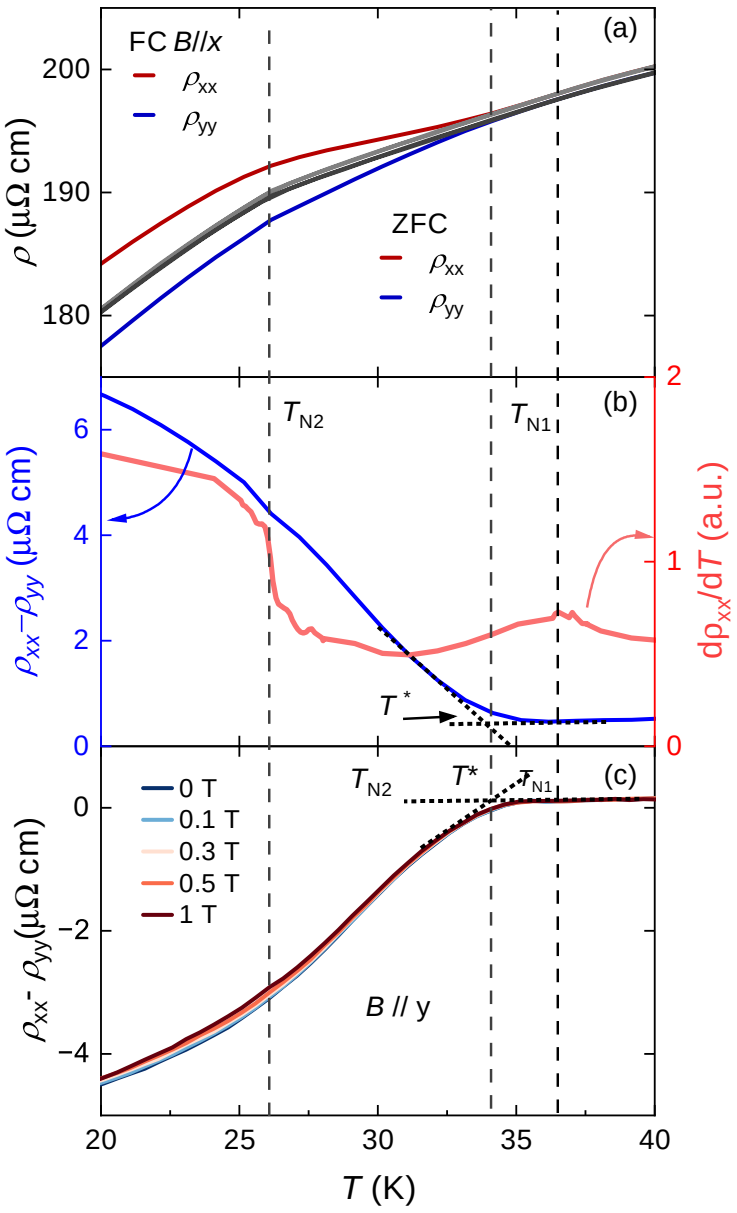

FIG. S16. **Comparison between nematic and magnetic transitions temperatures in a square-shape sample.** All data were measured by the Montgomery method. (a) ρ_{xx} and ρ_{yy} measured at zero magnetic field under ZFC and FC. For the FC state, the system is cooled from 50 K to 2 K under a magnetic field $\mu_0 H$=9 T along x axis. (b) Temperature evolution of resistivity anisotropy $\rho_{xx} - \rho_{yy}$ (left axis) and $d\rho_{xx}/dT$ (right axis). (c) Temperature dependence of $\rho_{xx} - \rho_{yy}$ under selected in-plane fields. Each curve was measured after cooling from 50 K to 2 K under $\mu_0 H = 9$ T applied along the y axis.

near the two magnetic transitions at T_{N1}= 37.0 K and T_{N2}= 26.1 K. $\Delta\rho_{yy}$ in Fig. S15(b,c) is the difference between $\rho_{yy}(FC)$ and $\rho_{yy}(ZFC)$; at zero field, $\Delta\rho_{yy}$ becomes finite below the nematic ordering temperature at $T^* \simeq 34$ K between T_{N1} and T_{N2}. Fig. S15(b) shows that T^* barely changes under a in-plane magnetic field. Figure S15(c) shows with out-of-plane magnetic fields, T^* gradually decreases and is fully suppressed above 4 T as shown in main text Fig. 4(b). Looking closely at $\rho_{yy}(FC)$ at zero field in Fig. S15(b,c), $\Delta\rho_{yy}$ shows a small kink at T_{N2}; this resembles the kink in the nematic order parameter near T_{N2} in our free energy simulation shown in main text Fig. 4(c).

T_{N1}, T_{N2} and T^* were also identified by a single measurement in a second sample (see Fig. S16, and the same data in Fig. S16(b) is also shown in main text Fig. 4(d,e)), where ρ_{xx} and ρ_{yy} are obtained by the Montgomery method. Fig. S16(a) shows that the system becomes anisotropic after field cooling. In Fig. S16(b), T_{N1} and T_{N2} can be determined by kinks in $d\rho_{xx}/dT$, while in contrast, T^* is determined by extrapolating the resistivity anisotropy $\rho_{xx}-\rho_{yy}$ from both the high-temperature background and the low temperature (upturn) region, with their intersection defined as T^* (see main text Fig. 4c). We also note that moderate in-plane magnetic fields barely modify $\rho_{xx}-\rho_{yy}$ as shown in Fig. S16(c). Given that the in-plane magnetic fields are found to act as a 'polarizing' force for the nematic domains, the in-plane-field-independence rules out that domain softness of the presumed antiferromagnetic order is responsible for the lower onset temperature of resistivity anisotropy relative to T_{N1}.

SUPPLEMENTARY REFERENCES

[S1] P. Park, W. Cho, C. Kim, Y. An, M. Avdeev, K. Iida, R. Kajimoto, and J.-G. Park, Composition dependence of bulk properties in the Co-intercalated transition metal dichalcogenide $Co_{1/3}TaS_2$, Phys. Rev. B **109**, L060403 (2024).

[S2] S. Parkin and R. Friend, 3*d* transition-metal intercalates of the niobium and tantalum dichalcogenides. I. magnetic properties, Philos. Mag. B **41**, 65 (1980).

[S3] S. Parkin and R. Friend, 3*d* transition-metal intercalates of the niobium and tantalum dichalcogenides. II. transport properties, Philos. Mag. B **41**, 95 (1980).

[S4] P. Park, Y.-G. Kang, J. Kim, K. H. Lee, H.-J. Noh, M. J. Han, and J.-G. Park, Field-tunable toroidal moment and anomalous hall effect in noncollinear antiferromagnetic weyl semimetal $Co_{1/3}TaS_2$, npj Quantum Materials **7**, 42 (2022).

[S5] A. Little, C. Lee, C. John, S. Doyle, E. Maniv, N. L. Nair, W. Chen, D. Rees, J. W. Venderbos, R. M. Fernandes, *et al.*, Three-state nematicity in the triangular lattice antiferromagnet $Fe_{1/3}NbS_2$, Nat. Mater. **19**, 1062 (2020).

[S6] M. Ye and A. V. Chubukov, Half-magnetization plateau in a heisenberg antiferromagnet on a triangular lattice, Phys. Rev. B **96**, 140406 (2017).

[S7] The basis function for E_2 irrep can be chosen as $\left(x^2-y^2, 2xy\right)$.

[S8] R. M. Fernandes, P. P. Orth, and J. Schmalian, Intertwined vestigial order in quantum materials: Nematicity and beyond, Annu. Rev. Condens. Matter Phys. **10**, 133 (2019).

[S9] H. Montgomery, Method for measuring electrical resistivity of anisotropic materials, J. Appl. Phys. **42**, 2971 (1971).

[S10] C. Dos Santos, A. De Campos, M. Da Luz, B. White, J. Neumeier, B. De Lima, and C. Shigue, Procedure for measuring electrical resistivity of anisotropic materials: A revision of the montgomery method, J. Appl. Phys. **110** (2011).

[S11] Z. Liu, Y. Shi, Q. Jiang, E. W. Rosenberg, J. M. DeStefano, J. Liu, C. Hu, Y. Zhao, Z. Wang, Y. Yao, *et al.*, Absence of E_{2g} nematic instability and dominant A_{1g} response in the kagome metal CsV_3Sb_5, Phys. Rev. X **14**, 031015 (2024).

[S12] K. A. Borup, K. F. F. Fischer, D. R. Brown, G. J. Snyder, and B. B. Iversen, Measuring anisotropic resistivity of single crystals using the van der Pauw technique, Phys. Rev. B **92**, 045210 (2015).

[S13] D. C. Jiles and D. L. Atherton, Theory of ferromagnetic hysteresis, J. Magn. Magn. Mater. **61**, 48 (1986).